Design, fabrication and cold test of a high-efficiency C-band travelling-wave accelerating structure[*]

Yihao Zhang,[1] Zhicheng Huang,[1] Yelong Wei,[1, †] Li Sun,[1] Zexin Cao,[1]
Chengzhe Wang,[1] Guangyao Feng,[1] Luigi Faillace,[2] and David Alesini[2]

[1]*National Synchrotron Radiation Laboratory, University of Science and Technology of China, Hefei, Anhui, 230029 China*
[2]*INFN Frascati National Laboratories, Frascati, Rome, Italy.*

To implement the linear injector for proposed Jinhua Light Source (JHLS) project, a 1-meter C-band constant gradient (CG) travelling wave (TW) accelerating structure is developed with the aim of to generate a gradient of $\geq$ 40 MV/m. This C-band structure works at a mode of $3\pi/4$ with a relatively low group velocity varying from 0.016c to 0.009c to increase the accelerating gradient at a given input power. It employs a cell shape with elliptical irises and circular arc tops to reduce the surface electric and magnetic fields and to achieve an average shunt impedance of 94 MΩ/m through optimizations. This results in an accelerating gradient of 40 MV/m with an input power of 29.6 MW, which has an efficiency comparatively higher than those of previously-reported C-band structures. Moreover, a new technique is utilized for the design of couplers, significantly simplifying the whole optimization process and achieves high accuracy. After fabrication, the structure was precisely tuned, results from low-power radiofrequency (RF) measurements and the comparison with simulated values are also presented in this paper.

Keywords: C-band, High-efficiency, Travelling-wave accelerating structure, New matching technique, Tuning method

I. INTRODUCTION

The S-band travelling-wave (TW) accelerating structures operating at 2.856 GHz or 2.998 GHz with a gradient of 20-30 MV/m [1, 2] are the most commonly used for various linear accelerators. However, the C-band and X-band accelerating structures are preferable for very compact linear accelerators, because both structures obtain smaller volume, higher shunt impedance and higher gradient as compared with S-band ones. Compared with the X-band accelerating structures, the C-band ones exhibit a larger iris aperture and a lower production precision [3, 4]. The beam-induced wakefield being reversely proportional to iris aperture might perturb the motion of the particles including emittance dilution and transverse instabilities [5]. The straightness tolerance is about $\pm$ 50 μm for a 1.8 m long C-band structure while it becomes close to $\pm$ 10 μm for the same structure operating at X-band. Therefore, the development of C-band accelerating structures is of particular interest.

The C-band accelerating structures were originally proposed and developed for upgrade of the KEKB injector linac at KEK in 2005. An accelerating gradient of 45 MV/m was firstly demonstrated for a C-band disk-loaded structure, which is twice of S-band accelerating structures [6, 7]. These C-band structures were subsequently implemented on a large scale at Spring-8 Angstrom compact free electron laser (SACLA) in the year of 2011. In SACLA 128 columns of the structure have been operated with an accelerating gradient of 35-38 MV/m at a maximum repetition rate of 60 Hz [8, 9]. In 2011, C-band technology with a gradient of 27 MV/m was also utilized to boost the beam energy from 0.38 GeV to 5.8 GeV at Swiss-FEL, Paul Scherrer Institute [10–12]. In 2020, the C-band technology with a gradient of 30-33 MV/m was successfully commissioned for the Shanghai XFEL facility [13, 14]. The comparisons of SACLA, Swiss-FEL and Shanghai XFEL are listed in Table 1 [8, 12, 14]. It should be noted here that these structures are designed for single-bunch mode, so HOM damping is not required. The linac of the European project Extreme Light Infrastructure-Nuclear Physics (ELI-NP) plans to use 12 C-band accelerating structures with HOM damping. An accelerating gradient of 33 MV/m has been successfully achieved for these HOM-damped structures at a repetition rate of 100 Hz [15]. The Jinhua Light Source (JHLS) is a proposed synchrotron radiation facility to be built at Jinhua, Zhejiang province, China in order to meet the increasing requirement of user demands for industrial applications. It consists of a linear injector, a booster and a storage ring. There are two critical considerations in the processing and production of accelerating structures for the linac. Firstly, we should obtain the target electron energy with the shortest possible acceleration length, which reduces the construction cost of the structure and its building. Consequently, it is imperative to employ high-gradient accelerating structures. Secondly, both surface electric and magnetic fields also increase with a higher accelerating gradient, thereby resulting in a higher breakdown rate (BDR). Therefore, it is crucial to achieve a high accelerating gradient with a low BDR. Two C-band undamped accelerating structures with an average gradient of 40 MV/m are employed to produce an electron beam energy of 150 MeV for the linear injector, as shown in Fig. 1. Both C-band structures are being developed by National Synchrotron Radiation Laboratory (NSRL) at University of Science and Technology of China (USTC).

For a periodic TW accelerating structure with a number of regular cells n, the accelerating gradient can be calculated as [16]

† Corresponding author, Yelong Wei, National Synchrotron Radiation Laboratory, University of Science and Technology of China, Hefei, Anhui, 230029 China, 17821183946,wylong@ustc.edu.cn.
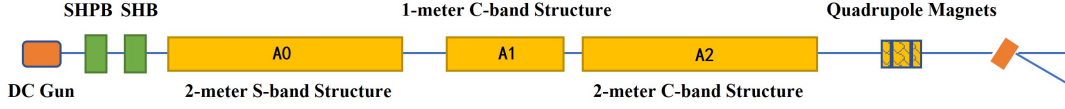
Fig. 1. Schematic of proposed Jinhua Light Source (JHLS) linear injector.

Table 1. Comparison of different undamped C-band structures.

Parameter	SACLA	Swiss-FEL	Shanghai XFEL	NSRL-JHLS
Frequency (GHz)	5.712	5.712	5.712	5.712
Working mode	$3\pi/4$	$2\pi/3$	$4\pi/5$	$3\pi/4$
Length (m)	1.8	2	1.8	1
Cell number	91	113	85	46
Average shunt impedance (MΩ/m)	54	80	62	94
Average gradient (MV/m)@input power (MW)	38@73	28@28.3	40@38.4	40@29.6
Efficiency (MV/m/$\sqrt{\text{MW}}$)	4.45	5.26	6.45	7.35

$$E_a(i) = \sqrt{\frac{\omega P_{\text{in}}(i) R_s(i)}{Q(i) v_g(i)}}, \qquad (1)$$

where $E_a(i)$, ω, $P_{\text{in}}(i)$, $R_s(i)$, $Q(i)$ and $v_g(i)$ represents the accelerating gradient, the working angular frequency, the input power, the shunt impedance, the quality factor and the group velocity for the ith cell ($i = 1, 2, 3, \ldots n$), respectively. It can be seen in Eq. (1) that a larger shunt impedance and a lower group velocity result in a higher accelerating gradient at a given input power. A key factor $K = E_a/\sqrt{P_{\text{in}}}$ can be used to denote the accelerating efficiency for a TW structure, where E_a represents the unloaded gradient at an input power of P_{in}. The larger the value of K, the higher efficiency a TW accelerating structure achieves. In order to facilitate a compact and high-efficiency linear injector for JHLS, a new C-band constant-gradient (CG) accelerating structure with a length of 1 meter is designed to produce a higher shunt impedance and a lower group velocity. As shown in Table 1, such a C-band structure has an efficiency higher than those previously-reported structures.

This paper presents the design, fabrication and cold test of our new C-band accelerating structure. It should be noted here that only 1-meter C-band structure is developed and reported in this paper. The rest of this paper is organized as follows: Sect. II describes the radiofrequency (RF) design of the C-band accelerating structure, including the optimizations on both regular cells and couplers. III introduces the fabrication and cold test results after tuning. Finally, Sect. IV summaries this paper.

II. RF DESIGN

This C-band accelerating structure consists of regular cells and couplers. In this section, we present the detailed optimizations on regular cells and couplers. A new technique combining improved Kyhl method with improved Kroll method is utilized for matching couplers to the accelerating structures with negligible reflections [17–21] and strong suppression of harmful multipole fields [5, 22]. This new C-band accelerating structure is designed according to the following criteria:

1. Based on existing C-band accelerating technology, we aim to obtain a shunt impedance of ≥ 90 MΩ/m and a high accelerating gradient of ≥ 40 MV/m.

2. A high surface electric field often leads to an increase of the BDR in the accelerating structure. Special attention should be paid to ensure that the surface electric field is below the breakdown threshold.

3. A high surface magnetic field resulting in a high temperature rise due to pulsed heating often limits the achievable accelerating gradient. The calculated pulsed temperature rise should be lower than 40 K in order to keep a low BDR.

4. The water-cooling method should be carefully designed to ensure that it is able to cope with the heat load of this structure and thus ensure the accuracy of the accelerating phase.

A. Regular Cells

To meet the above-mentioned criteria, Computer Simulation Technology (CST) software [23] is used for our optimizations. In the design of the regular cells for the accelerating structure with an accelerating gradient E_a, three quantities of surface fields are usually investigated: normalized E_s/E_a, H_s/E_a, and S_c/E_a^2, where E_s and H_s represent the surface electric field and magnetic field, respectively, and $S_c = |\text{Re}(\vec{S})| + \frac{1}{6}|\text{Im}(\vec{S})|$ represent the surface modified Poynting factor [24]. The regular cell is chosen to have a shape with elliptical irises and circular arc tops to reduce the surface electric field and enhance the shunt impedance [25], as shown in Fig. 2(a).

The working mode of phase advance is related to the group velocity, quality factor and the shunt impedance [26]. Different modes of phase advance are listed and compared in Table 2 when employing fixed cell parameters of $a = 5.7415$ mm, $a_e = 1.25$ mm, $b_e = 1.8$ mm, $R = 7$ mm. It can be seen that as the phase advance increases, the quality factor increases while the group velocity decreases, and $3\pi/4$ mode

has the highest shunt impedance. After considering RF parameters of all these modes, $3\pi/4$ mode is chosen to be the working mode.

Table 2. Comparison of different undamped C-band structures.

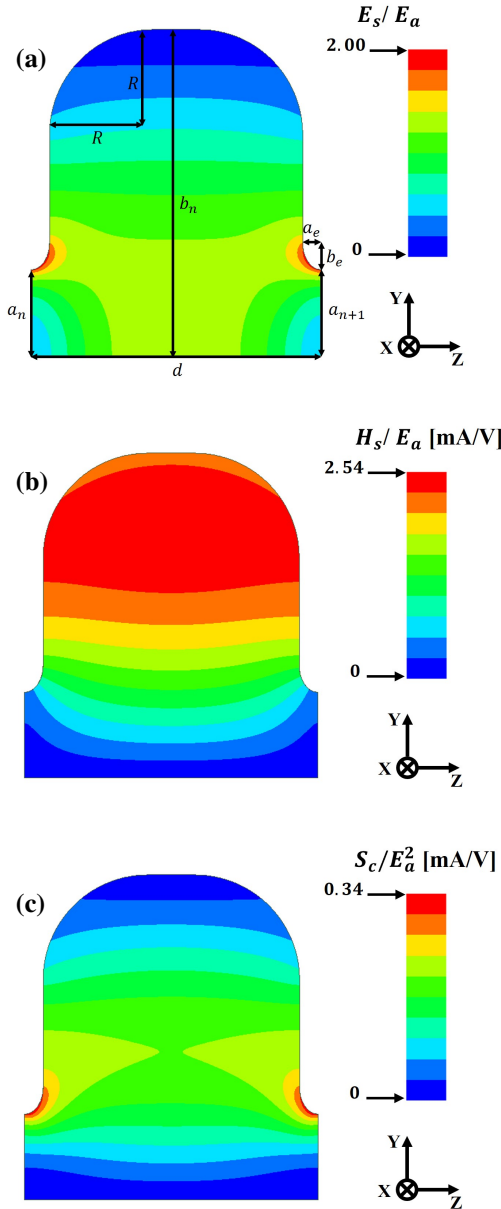| Parameter	$2\pi/3$	$3\pi/4$	$4\pi/5$
Frequency (GHz)	5.712	5.712	5.712
Quality factor	11011	11991	12500
v_g/c (%)	1.469	1.199	0.996
R_s (MΩ/m)	92.7	93.9	92.9

Fig. 2. Simulated distributions of surface electric field E_s/E_a **(a)**, magnetic field H_s/E_a **(b)**, and modified Poynting factor $S_c/(E_a^2)$ **(c)** for the middle cell.

It is of particular importance to choose the iris radius of the cell. A larger iris radius may result in a higher group velocity and more effective suppression of short-range wakefield [5, 26]. The iris radius of $a = 5.233-6.25$ mm is chosen for our C-band CG structure from consideration of the beam dynamics requirement in JHLS linear injector. Through optimizations, for the middle cell with an iris radius $a = 5.7415$ mm, the surface electric field, magnetic field, and modified Poynting factor are shown in Fig. 2. Table 3 gives the optimum RF properties of the first, middle, and end cell. The v_g/c and R_s/Q denote the group velocity normalized to the speed of light c and the shunt impedance R_s over quality factor Q, respectively.

Table 3. RF properties of the first, middle, and end cell.

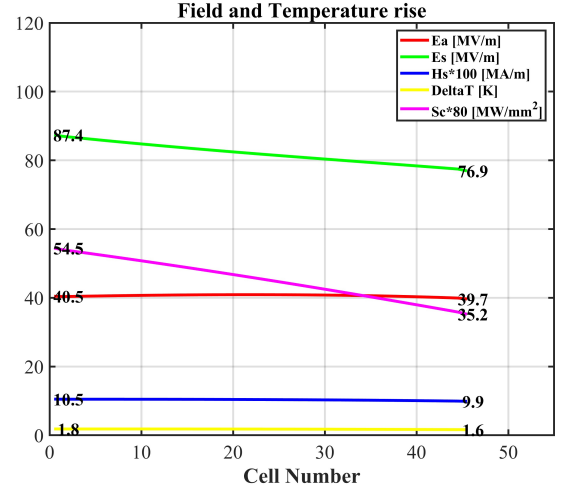| Parameter	First cell	Middle cell	End cell
Iris radius (mm)	6.25	5.7415	5.233
Frequency (GHz)	5.712	5.712	5.712
Quality factor	12001	11991	11950
v_g/c (%)	1.6013	1.1988	0.8654
R_s/Q (Ω/m)	7400	7829	8220
E_s/E_a	2.16	2.00	1.94
H_s/E_a (mA/V)	2.6	2.54	2.49
S_c/E_a^2 (mA/V)	0.416	0.34	0.28

Fig. 3. Interpolated E_a, E_s, H_s, S_c and pulsed temperature rise ΔT as a function of cell number for the whole structure.

The pulsed heating resulting from the surface magnetic field is expressed as follows [27–29]:

$$\Delta T = 127|H_s|^2 \sqrt{f t_p}, \qquad (2)$$

where H_s, f, and t_p represent the surface magnetic field in MA/m, the RF frequency in GHz, the RF pulse length in μs, respectively. A practical criterion from experiments is that the temperature rising due to pulsed heating should be less than 40∼50 °C to avoid BDR rising [30]. A RF pulse length of 0.3 μs is utilized to calculate the pulse heating for our structure consisting of only regular cells. The RF properties of other

regular cells can be interpolated using the data from the first, middle, and end cells. Figure 3 shows the interpolated RF properties for our structure. It can be seen in Fig. 3 that the maximum temperature rise is calculated to be 1.8 K, which is much lower than that of other C-band structures. This means that the accelerating gradient of ≥ 40 MV/m can be achieved without breakdown due to pulsed heating.

B. Couplers

It is of particular importance to carefully design the couplers so that RF power is smoothly transmitted into and out of the structure with negligible reflections. Couplers can be defined as "electric" or "magnetic" coupling depending on which type of field is used for coupling [22, 31]. A TW accelerating structure consists of a number of regular cells and two couplers. Each coupler includes a waveguide and a matching cell. The matching cells are used to achieve matching between the waveguides and the regular cells.

To ensure a good beam quality, excellent homogeneity of the accelerating field is required. However, coupled slots can lead to distortions in the field distribution, multipole components might dilute the beam emittance [22]. Therefore, the design of the coupler is mainly concerned with optimizations on matching cells and suppression of multipole components.

The magnetic couplers are utilized to smoothly transfer RF power into and out of our C-band structure. Both couplers are designed by a new technique combining both improved Kyhl method and improved Kroll method, greatly reducing the simulation time while maintain accuracy. The details on the design of couplers can be found in [21, 32]. A first short C-band structure with 4 regular cells connected to an input coupler and an output coupler is modelled for the simulations, as shown in Fig. 4. It should be noted here that the regular cells are the four last cells adjacent to the output matching cell while the input coupler is only for this short structure rather than for the whole structure.
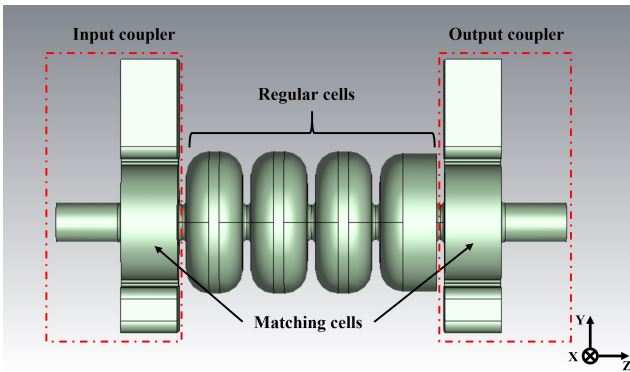

Fig. 4. A modelling of a short C-band structure with an input coupler, four regular cells, and an output coupler.

The local reflection coefficient $20\log|R'|$ can be optimized to be lower than -50 dB by adjusting the coupling aperture a_{co} and cell diameter b_{co} for the output coupler. In this case, RF power can propagate of the output waveguide with negligible reflections. After the optimizations on the output coupler for the whole structure, the same approach is also used to design the input coupler. A second short C-band structure consisting of an input coupler, four regular cells and an output coupler is modelled for the simulations. In this case, the regular cells are the four first cells adjacent to the input matching cell while the output coupler is only for this short structure rather than for the whole structure. Through sweeping different coupling aperture a_{ci} and matching cell diameter b_{ci}, the global reflection coefficient $|S_{11}|$ can be minimized to be lower than -50 dB at the input waveguide. The on-axial longitudinal electric field distribution for both optimum short structures is shown in Fig. 5.
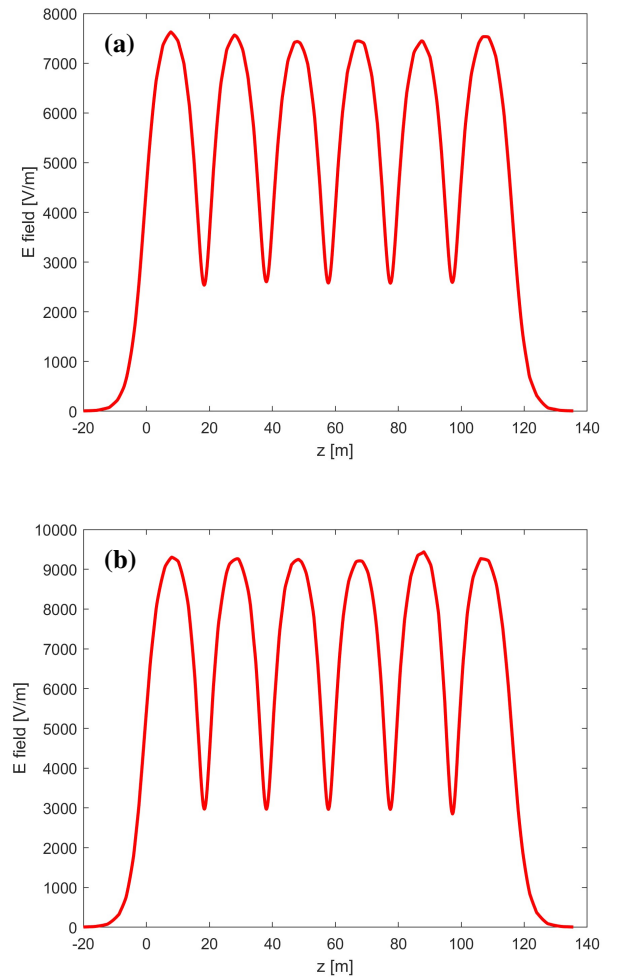

Fig. 5. Electric field distribution for the first short structure (a) and for the second short structure (b).

To suppress the dipole field components in the couplers, one straightforward way is to use a symmetric feed (it is also called as dual-feed), but it may result in a high cost and complexity for the fabrication. Here a single input coupler with a short-circuited rectangular waveguide is employed for our structure due to a low fabrication cost [22, 33]. Through ad-

justing waveguide height H (see Fig. 6), the dipole field components can be greatly reduced to a very low level. However, the quadrupole field components still exist in the couplers. A coupler with racetrack geometry can be used to suppress the quadrupole field components [5, 22]. This racetrack shape employs two circles with an eccentric distance of Δx. The quadrupole field components can be strongly suppressed by adjusting Δx. The adjustment of Δx also has an effect on the dipole field components, but this effect is very weak and can be neglected. So it can be assumed that the suppression processes of the dipole field components and the quadrupole field components are independent to each other. The methods and procedures of calculating the remaining dipole and quadrupole field components are detailed in [33].

After optimizations, the remaining multipole field components at the input and output couplers are presented in Table 4. It should be noted here that the multipole field components are calculated relative to the monopole electric field components along the center axis.
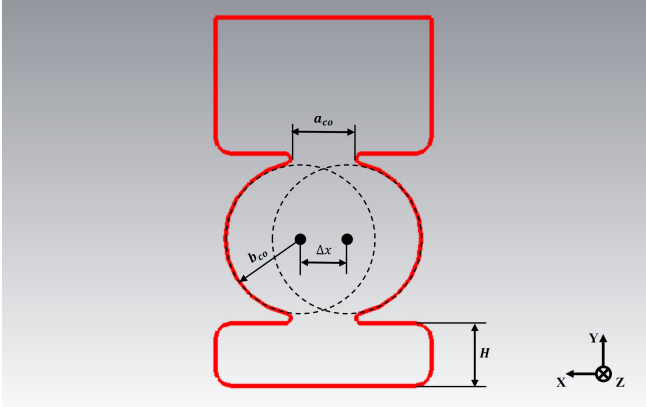

Fig. 6. Cross-sectional view of the couplers.

Table 4. Remaining multipole components at the input and output couplers relative to the monopole electric field components along the center axis.

Coupler type	Dipole	Quadrupole
Input coupler (%)	0.046	0.036
Output coupler (%)	0.058	0.087

C. The Entire Structure

To evaluate the design performance, the entire structure is then modeled. It should be noted that due to the regular cells and the couplers were processed through different machining methods in the workshop, in order to ensure the machining accuracy as well as to facilitate brazing, both the first and end regular cells have a shape of a cup-like. A RF pulse length of 0.3 μs is utilized for it, so the maximum surface magnetic field should not exceed 0.49 MA/m according to Eq. (2).
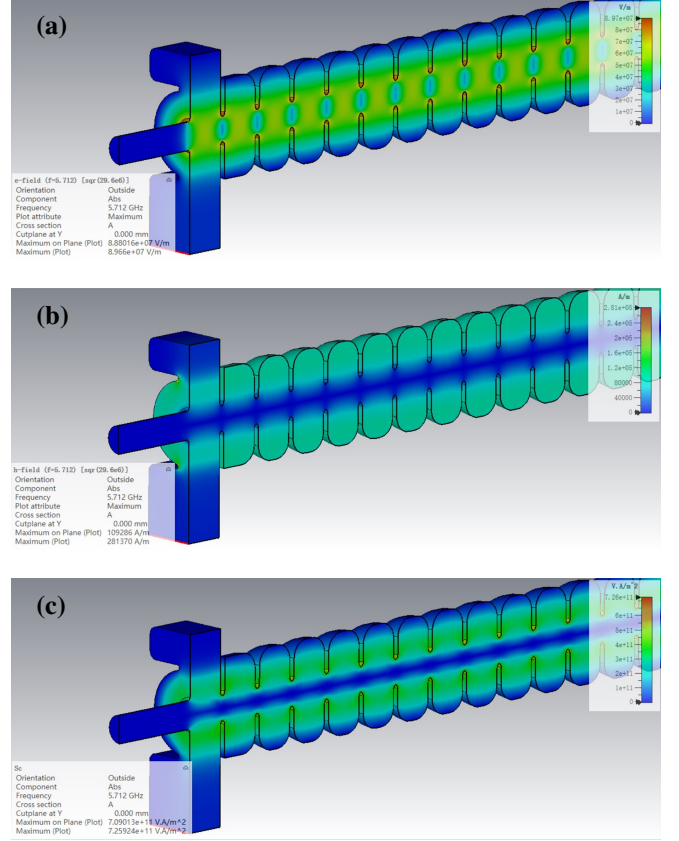

Fig. 7. Surface electric field E_s **(a)**, surface magnetic field H_s **(b)**, and modified Poynting factor S_c **(c)** at 29.6 MW of incident power simulation results from CST.

When our structure is driven by an input power of 29.6 MW an accelerating gradient of 40 MV/m can be generated. In this situation, the surface electric field, magnetic field, and modified Poynting factor are simulated for the whole structure, as shown in Fig. 7. The disadvantage of adopting a racetrack shape coupler is that the surface magnetic field H_s increases relative to a normal shape coupler, especially at the neck of the coupler. It can be clearly seen in Fig. 7(b) that the maximum surface magnetic field of 0.28 MA/m (much higher than the interpolated value of 0.105 MA/m) is located at the neck of the coupler at target operating power, but it is still lower than the computational threshold of 0.49 MA/m. This ensures that BDR will not increase because of pulsed heating. Based on these optimizations, the RF parameters for our entire C-band structure are listed in Table 5.

The phase advance is defined as the difference in phase between a selected cell and the next adjacent cell. The accuracy of the phase advance in the regular cells has a great impact on the accelerating voltage for the electron beam to experience. The phase stability [26] is an important quantity to influence the performance of a TW accelerating structure. It can be estimated using $d\varphi/df = 2\pi t_f/n$, where φ, t_f, n represents the phase advance of the periodic cell, the filling time and the number of cells, respectively. So we can calculate the phase stability of the structure to be 1.98°/MHz according to the pa-

rameters in Table 5. For an accelerating structure powered by a klystron, the primary cause of frequency fluctuations is the temperature variation of the water-cooling system [34]. An increase in the heat load of the accelerating structure can result in thermal expansion of the cell and change the cell's resonant frequency. We designed the resonant frequency of the regular cell to be 5712 MHz at a temperature of 30 °C, and the allowed RF phase jitter is less than $\pm 0.5°$. To estimate the frequency offset and phase change, Oxygen Free Copper is selected by ANSYS [35] to simulate the temperature distribution as well as the thermal expansion of the accelerating cell. Our simulated thermal design predicts an average heat load of 10.1 W for a single cell when an input RF power of 29.6 MW is fed to the accelerating structure. A water-cooling method is carefully designed for the structure to efficiently transfer the heat and mitigate thermal expansion and frequency shift of the regular cells. Six water channels with an inner diameter of 8 mm are placed inside the structure. To minimize the temperature gradient along the accelerating structure, the counterflow method is employed.

Figure 8 shows the simulated temperature distribution of the middle cell for the structure at an average temperature of 30 °C as the designed resonant frequency of 5712 MHz. With a cooling water temperature of 27.5 °C at an inlet, the temperature of the structure can be maintained at 30 °C. The maximum temperature at the surface of the regular accelerating cell is 31.5 °C. The diameter ($2b$) of the cell increases by approximately 0.44 μm, resulting in a decrease of the cavity resonant frequency from 5712 MHz by 64.5 kHz, which corresponds to a 0.13° change in the phase advance, less than 0.5°. This indicates that the phase stability of the structure meets the design requirements.
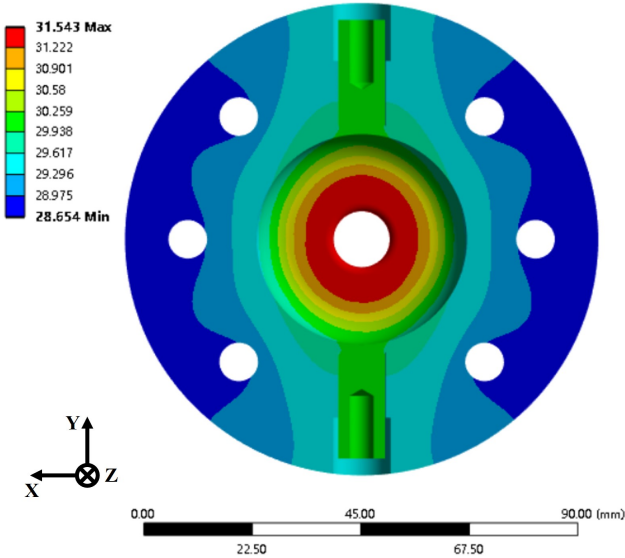
III. MECHANICAL FABRICATION AND TUNING

This accelerating structure is made of Oxygen Free Copper with a low resistive RF power loss. Different with the traditional disk-loaded structure, the regular cells are lathed because of elliptical fillets and curved tops while the couplers are milled. The mechanical units before brazing are shown in Fig. 9(a). The tolerances for all of dimensions are controlled to be within 5 μm and the surface roughness should not be exceeding 0.2 μm. Fig. 9(b) shows a regular three-dimensional (3D) mechanical unit model for fabrication. It contains a full iris as well as parts of the two cells on both sides. Each cell has two tuning holes on both sides, with the stress areas at the straight part. Two tuning holes are located in straight sections on each side of a single cell, therefore the force generated by pushing or pulling during tuning is perpendicular to the cell. Due to the constraints imposed by the machining conditions described in the preceding section, the first and last 3D mechanical units are shown in Fig. 9(c) and 9(d), respectively. A 3D model for the entire structure and a photograph of the fabricated prototype are presented in Fig. 10. After brazing a vacuum leakage test and a hydraulic resistance test were conducted to check for vacuum leaks in the regular cells and the couplers, as well as water leaks in the cooling-water channels.
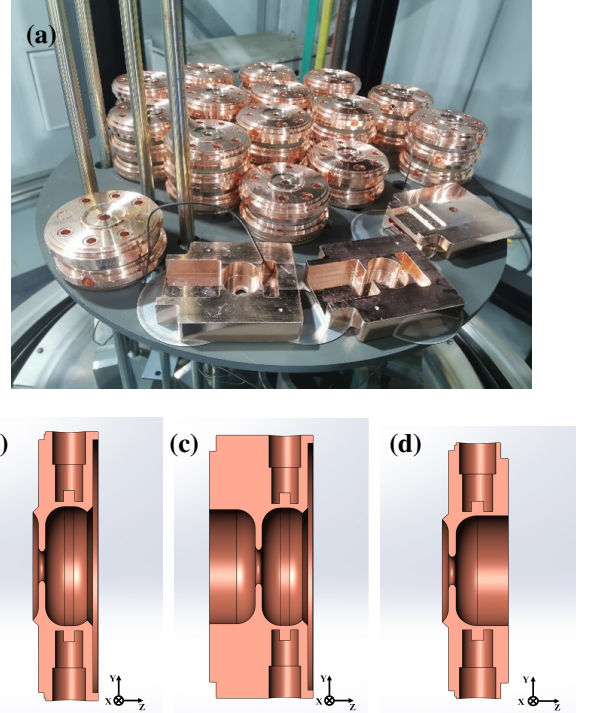

Fig. 9. The fabricated mechanical units before brazing (a) and 3D mechanical units (b-d).

Fig. 8. Simulated temperature distribution of the middle accelerating cell when an input power of 29.6 MW is fed to the accelerating structure.

The machining errors degrade the performance of the entire structure. So the fabricated prototype structure has to be put for tuning. Here our tuning is performed using the nodal-shift method while the field distributions of the tuned structure are measured using the bead-pull method [36–39]. A E5071C

Table 5. Design parameters of the whole C-band structure.

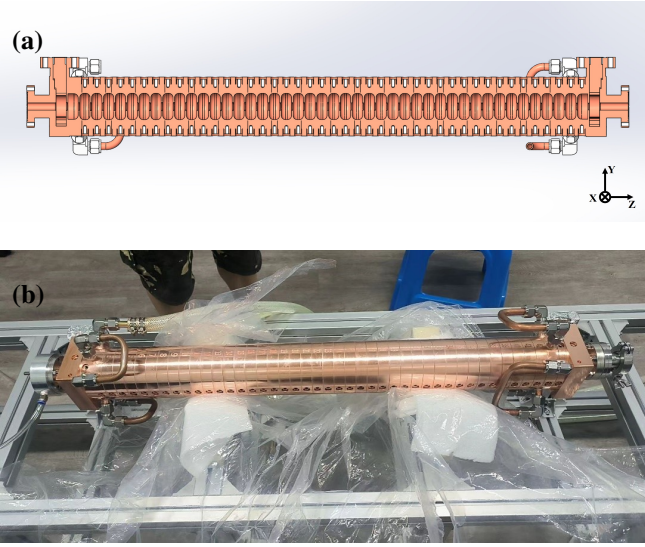| Parameter		Value	Unit
Working frequency	f	5712	MHZ
Working mode		$3\pi/4$	rad
Number of cells		44+2	
Cell length	d	19.682	mm
Disk thickness	$2a_e$	2.5	mm
Iris diameter	$2a$	12.5∼10.466	mm
Cell diameter	$2b$	43.837∼43.374	mm
Shunt impedance	R_s	89.6∼98.5	MΩ/m
Quality factor	Q	12022∼11959	
Group velocity	v_g/c	1.60%∼0.865%	
Filling time	t_f	253	ns
Attenuation factor	τ	0.3781	
Maximum surface electric field	E_s/E_a	2.24	
Maximum surface magnetic field	H_s/E_a	7.02	mA/V
Maximum surface modified Poynting factor	S_c/E_a^2	0.45	mA/V

(a)

(b)

Fig. 10. 3D model **(a)** and photograph of the fabricated prototype **(b)** for the entire structure after brazing.

the relative magnitude of the onxial electric field at the center of structure. It can be seen that the peak field points present a periodic change and are presumably constant.
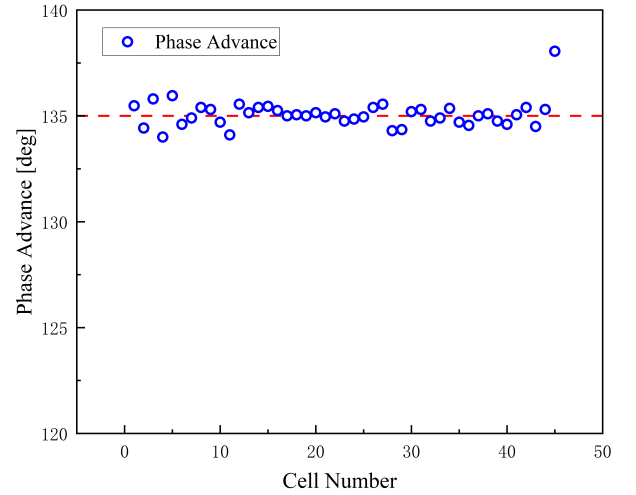

Fig. 11. Phase advance between adjacent cells after tuning.

Vector Network Analyzer (VNA) is selected for the cold tuning.

The nodal-shift method introduces a metallic tuner moved to the center of the accelerating cells so that they are short-circuited or detuned. In this case, the reflection coefficient due to this detuning is purely imaginary and can be compensated for by changing the resonant frequency of the cell. The short-circuit metallic tuner is moved from cell to cell so that the measured phase advances of the adjacent cells are maintained in 135° by directly tuning the regular cells. This tuning method is not affected by whether the output coupler is matched or not, but should be performed after the input coupler is tuned.

Figure 11 shows the phase advance between adjacent cells after tuning by the nodal-shift method. Each phase advance per cell is within the range 135°±1°, except the last cell is tuned for achieving an acceptable field flatness. Fig. 12 shows

The S-parameters for the entire structure were measured after tuning, as shown in Fig. 13. At the working frequency 5.712 GHz, the reflection $|S_{11}|$ and transmission $|S_{21}|$ are measured to be -43 dB and -3.48 dB, respectively. The measured transmission $|S_{21}|$ has a good agreement with simulation values of -3.4 dB. The bandwidth of reflection below -30 dB is 2.74 MHz. The filling time is also measured by the VNA, and the results are displayed in Fig. 14. The exact measured value is 255.5 ns, the average group velocity can be calculated from this value by $v_g = L/t_f = 1.18\%c$. The measured group velocity is lower than the design value, which indicates that the iris diameters of the cells are smaller than the designed value. The quality factor can be obtained by using Eq. (3):
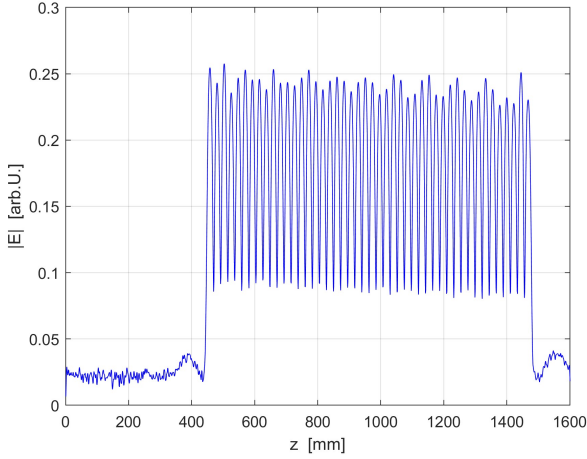
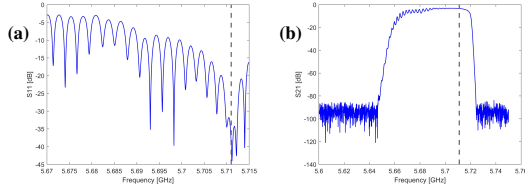Fig. 12. Relative magnitude of the electric field after tuning.

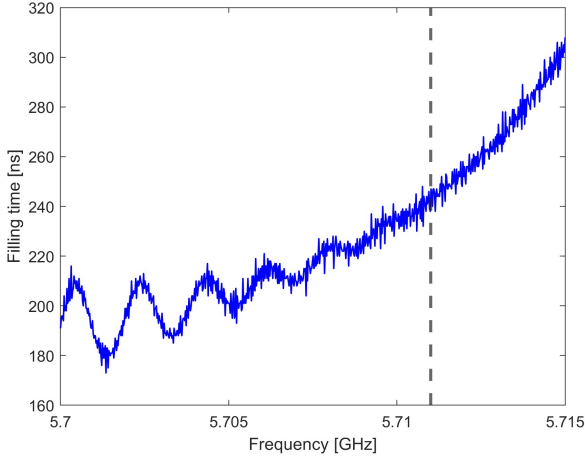Fig. 13. S_{11} and S_{21} for the entire structure after tuning.

Fig. 14. Filling time after tuning.

$$Q = \frac{\pi f t_f}{-\ln(|S_{21}|)} \qquad (3)$$

Where f is the working frequency, t_f denotes the filling time, $|S_{21}|$ presents the magnitude of S_{21}. Bringing in the values, the quality factor is calculated by Eq. (3) to be 11443, 4.6% reduction compared to the simulation value 12000. The comparison of the measured results and simulated RF parameters is presented in the Table 6.

Table 6. Comparison of measured and simulated values.

Parameter	Measured	Simulated
Reflection coefficient S_{11} (dB)	-43	<-40
Transmission coefficient S_{21} (dB)	-3.48	-3.4
Filling time t_f (ns)	255.54	253
Group velocity v_g/c (%)	1.18	1.22
Quality factor Q	11443	12000

IV. SUMMARY

In this paper, a 1-meter high-efficiency C-band constant-gradient TW accelerating structure operating at $3pi/4$ mode has been developed at NSRL, USTC for JHLS project. Such a structure is designed to generate an accelerating gradient of 40 MV/m with an input power 29.6 MW. The regular cell is chosen to have a shape with elliptical irises and circular arc tops to reduce the surface electric field and enhance the shunt impedance. A new matching strategy combining with improved Kyhl method and improved Kroll method is also used for the coupler design, which greatly reduces the simulation time while maintaining a high accuracy. A racetrack and a short-circuit waveguide are also introduced to heavily suppress the multipole components. After fabrication the structure was precisely tuned and cold-tested using the nodal-shift method and bead-pull method, achieving a global reflection coefficient of -43 dB at the working frequency of 5.712 GHz. The measured parameters are consistent with our designed ones. In the next step, the high-power conditioning is planned to be conducted to see whether the target gradient of 40 MV/m can be obtained for this structure. This will be reported in separate publications.

[1] C. Tang, W. Huang, R. Li et al., Tsinghua Thomson scattering X-ray source. Nucl. Instrum. Methods Phys. Res. Sect. A **608**, S70–S74 (2009). https://doi.org/10.1016/j.nima.2009.05.088

[2] Y. Jiao, G. Xu, X.H. Cui et al., The HEPS project. J Synchrotron Rad **25**, 1611–1618 (2018). https://doi.org/10.1107/S1600577518012110

[3] JR. Zhang, YL. Chi, J, Lei et al., Design of a C-band Travelling-wave Accelerating Structure at IHEP, *in Proceedings of IPAC2017* (2017).

[4] T.G. Lucas, X.F.D. Stragier, P.H.A. Mutsaers et al. RF design of a compact, X-band travelling-wave RF photogun made from halves. Nucl. Instrum. Methods Phys. Res. Sect. A **1013**, 165651 (2021). https://doi.org/10.1016/j.nima.2021.165651

[5] Q. Gao, H. Zha, J. Shi et al. Design and test of an X-band constant gradient structure. Phys Rev Accel Beams **27**, 090401 (2024).

https://doi.org/10.1103/PhysRevAccelBeams.27.090401

[6] T.S.T. Shintake, The Choke Mode Cavity. Jpn J Appl Phys **31**, L1567 (1992). https://doi.org/10.1143/JJAP.31.L1567

[7] T. Kamitani, T. Sugimura, K. Yokoyama et al., Status of C-band accelerator module in the KEKB injector LINAC, *in Particle Accelerator Conference* (2009). https://doi.org/10.1109/PAC.2007.4440570

[8] T. Inagaki, C. Kondo, H. Maesaka et al., High-gradient C -band linac for a compact x-ray free-electron laser facility. Phys Rev ST Accel Beams **17**, 080702 (2014). https://doi.org/10.1103/PhysRevSTAB.17.080702

[9] T. Sakurai, H. Ego, T. Inagaki et al., C -band disk-loaded-type accelerating structure for a high acceleration gradient and high-repetition-rate operation. Phys Rev Accel Beams **20**, 042003 (2017). https://doi.org/10.1103/PhysRevAccelBeams.20.042003

[10] S. Reiche, P.S. Institut, Status of the SwissFEL Facility at the Paul Scherrer Institute, *in Proceedings of FEL* (2011).

[11] F. Loehl, F. Löhl, J. Alex et al. Status of the SwissFEL C-band Linear Accelerator, *in Proceedings of FEL* (2013).

[12] J.Y. Raguin, The Swiss FEL C-Band Accelerating Structure: RF Design and Thermal Analysis, *in Proceedings of LINAC2012* (2012).

[13] M. Zhang, Q. Gu, New linear accelerator (Linac) design based on C-band accelerating structures for SXFEL facility. Chinese Phys C **35**, 066–1069 (2011). https://doi.org/10.1088/1674-1137/35/11/016

[14] W. Fang, Q. Gu, X. Sheng et al., Design, fabrication and first beam tests of the C-band RF acceleration unit at SINAP. Nucl. Instrum. Methods Phys. Res. Sect. A **823**, 91–97 (2016). https://doi.org/10.1016/j.nima.2016.03.101

[15] D. Alesini, M. Bellaveglia, F. Cardelli et al., Realization and high power test of damped C-band accelerating structures. Phys Rev Accel Beams **23**, 042001 (2020). https://doi.org/10.1103/PhysRevAccelBeams.23.042001

[16] T. P. Wangler, *RF Linear accelerators*. (Wiley-VCH Verlag GmbH & Co. KGaA, 2008), pp. 74–76.

[17] E. Westbrook, Microwave Impedance Matching of Feed Waveguides to the Disk-Loaded Accelerator Structure Operating in the $2\pi/3$ Mode, Technical Report No. SLAC-TN-63-103 (Stanford Linear Accelerator Center, 1963).

[18] M. Chanudet, Matching of the Coupler Cavity to Travelling Wave Structures at any Operating Mode, Technical Report No. LAL-RT 93-06 (Laboratoire de l'Accélérateur Linéaire, 1993).

[19] S. Zheng, Y. Cui, H. Chen et al. A quantitative method of coupler cavity tuning and simulation, *in Particle Accelerator Conference* (2001). https://doi.org/10.1109/PAC.2001.986547

[20] N.M. Kroll, Applications of Time Domain Simulation to Coupler Design for Periodic Structures, *in Proceedings of the 20th International Linac Conference* (2000). https://doi.org/10.2172/765007

[21] Z. Huang, Y. Wei, Z. Cao et al., New design techniques on matching couplers for travelling-wave accelerating structures. Phys Rev Accel Beams **27**, 082001 (2024). https://doi.org/10.1103/PhysRevAccelBeams.27.082001

[22] D. Alesini, Power coupling. arxiv preprint, arxiv:1112.3201 (Laboratori Nazionali di Frascati, 2011).

[23] CST STUDIO SUITE. https://www.cst.com

[24] A. Grudiev, S. Calatroni, W. Wuensch, New local field quantity describing the high gradient limit of accelerating structures. Phys Rev ST Accel Beams **12**, 102001 (2009). https://doi.org/10.1103/PhysRevSTAB.12.102001

[25] R. Zennaro, J. Alex, M. Bopp et al., Conceptual design of the C-band module for the SwissFEL, *in Proceedings of LINAC2010*, (2010).

[26] W. Fang, Q. Gu, D. Tong et al., Design optimization of a C-band traveling-wave accelerating structure for a compact X-ray Free Electron Laser facility. Chin Sci Bull **56**, 3420–3425 (2011). https://doi.org/10.1007/s11434-011-4754-y

[27] D.P. Pritzkau, RF pulsed heating (Doctoral dissertation, Stanford University, 2001). https://doi.org/10.2172/798978

[28] D. P. Pritzkau, R.H. Siemann, Experimental study of rf pulsed heating on oxygen free electronic copper. Phys Rev ST Accel Beams **5**, 112002 (2002). https://doi.org/10.1103/PhysRevSTAB.5.112002

[29] L. Laurent, S. Tantawi, V. Dolgashev et al., Experimental study of rf pulsed heating. Phys Rev ST Accel Beams **14**, 041001 (2011). https://doi.org/10.1103/PhysRevSTAB.14.041001

[30] F. Wang, C. Adolphsen, C. Nantista, Performance limiting effects in X -band accelerators. Phys Rev ST Accel Beams **14**, 010401 (2011). https://doi.org/10.1103/PhysRevSTAB.14.010401

[31] C. Nantista, S. Tantawi, V. Dolgashev, Low-field accelerator structure couplers and design techniques. Phys Rev ST Accel Beams **7**, 072001 (2004). https://doi.org/10.1103/PhysRevSTAB.7.072001

[32] Z. Huang, Y. Wei, Z. Cao et al., Simulations Design of a C-band Travelling-wave Accelerating Structure, *in Proceedings of the 2024 IEEE International Conference on Computational Electromagnetics* (2024). https://doi.org/10.1109/ICCEM60619.2024.10559107

[33] S. Ma, F. Wu, Z. Wang et al., Design and tuning of S-band traveling wave accelerating structures for Hefei Advanced Light Facility. Review of Scientific Instruments **95**, 103301 (2024). https://doi.org/10.1063/5.0208801

[34] X.-C. Lin, H. Zha, J.-R. Shi et al., Design, fabrication, and testing of low-group-velocity S-band traveling-wave accelerating structure. NUCL SCI TECH **33**, 147 (2022). https://doi.org/10.1007/s41365-022-01124-9

[35] ANSYS. http://ansys.com.

[36] W. Fang, D. Tong, Q. Gu et al., Design and experimental study of a C-band traveling-wave accelerating structure. Chin Sci Bull **56**, 18–23 (2011). https://doi.org/10.1007/s11434-010-4265-2

[37] D. Alesini, A. Citterio, G. Campogiani et al., Tuning procedure for traveling wave structures and its application to the C-Band cavities for SPARC photo injector energy upgrade. J Inst **8**, P10010 (2013). https://doi.org/10.1088/1748-0221/8/10/P10010

[38] C.W. Steele, A Nonresonant Perturbation Theory. IEEE Transactions on Microwave Theory and Techniques **14**, 70–74 (1966). https://doi.org/10.1109/TMTT.1966.1126168

[39] J. Shi, A. Grudiev, W. Wuensch et al., Tuning of X-band traveling-wave accelerating structures. Nucl. Instrum. Methods Phys. Res. Sect. A **704**, 14–18 (2013). https://doi.org/10.1016/j.nima.2012.11.182